



High-precision camera calibration based on concentric circle compensation for industrial environments

TAO PENG, ANQI GU, DUJUAN FANG, AND ZHIJIANG ZHANG*

School of Communication and Information Engineering, Shanghai University, Shangda Road 99, Shanghai, China

*zjzhang@shu.edu.cn

Abstract: Accurate calibration of cameras in industrial production vision systems is a critical fundamental task. However, industrial visual measurement systems often face challenges such as large fields of view, shallow depths of field, and the use of imprecise large calibration templates. These factors make the task of accurate visual measurement in the industrial production environment a great challenge. This paper presents a camera calibration algorithm based on the eccentricity error of concentric circles and the fixed topological relationship constraints of the calibration board structure. In this calibration algorithm, the homography relationship of the calibration board targets is calculated to iteratively optimize the eccentricity error of the concentric circle patterns, providing stable and accurate feature point information for precise camera calibration in industrial settings. Additionally, during the iterative calibration process, deviation parameters are introduced for each feature point on the calibration board relative to the standard plane to account for the machining and geometric deformation errors of the calibration board. This approach addresses issues related to the imprecise calibration of large planar templates. These deviation parameters and eccentricity errors of the concentric circle feature points are optimized together with the camera calibration parameters to correct the positions of the feature points and enhance the camera calibration accuracy in complex industrial scenarios. The results of simulation and experiments validate the feasibility and operability of the proposed camera calibration method. It can fundamentally eliminate perspective transformation errors and improve the precision of camera parameters and target geometry.

© 2025 Optica Publishing Group under the terms of the [Optica Open Access Publishing Agreement](#)

1. Introduction

Camera calibration is a core technology of vision system applications. In particular, when these systems are used for measurements at various scales, the accuracy of the camera calibration serves as a benchmark for the measurement precision that the entire visual measurement system can achieve [1]. This process uses calibration templates to solve the projective transformation relationship between the visual measurement system and the measurement target. The precise extraction of control points on the calibration template and their corresponding image points directly affects both the calibration precision and the robustness [2].

To address position errors caused by the extraction of image points from control points on the calibration template, Datta [3] proposed a method that utilizes iterative updates to extract target feature points. Liu [4] improved the accuracy of the camera calibration for low-cost cameras by introducing image perturbation factors into each target image feature point on a checkerboard calibration board. They established the image projection error as a minimal objective function based on the homography matrix between the target plane and the image plane. Thus, the optimal coordinates of all image feature points can be obtained by nonlinear optimization. Song [5] used an unbiased estimator. Projection and matrix changes during distortion are tracked to accurately detect subpixel feature point coordinates of distorted circular patterns. Although these methods

improve the precision of feature point extraction, the accuracy of extraction is significantly affected during the image transformation process, which reduces the overall calibration precision.

Regarding manufacturing errors in calibration targets, Strobl [6] preset the geometric values of three nonlinear feature points on a checkerboard pattern during monocular camera calibration. Meanwhile, the camera parameters and target geometry are estimated. Huang [7] proposed a planar constraint optimization method based on a virtual ideal plane error model to improve the accuracy of camera calibration. The deviation parameters relative to the virtual ideal plane were added to each feature point to optimize the positions of calibration feature points. However, the constraints upon which this research is based may be difficult to implement in real scenarios. When dealing with calibration targets that deviate from the ideal plane and exhibit irregularities, it is difficult to achieve the expected calibration results.

Existing research indicates that using two-dimensional plane templates for calibration of vision measurement systems in industrial settings is a common choice. Calibration control points on these templates include checkerboards [8–10], deltill corner [11], fan-shaped target [12], ArUco-encoded board [13,14], circles [15–17], and concentric circles [18–20]. Although checkerboard patterns are efficient for corner point localization, their accuracy and stability can be significantly compromised in industrial environments due to motion blur and environmental interference. In contrast, circular or ring patterns possess clear geometric constraints. So, it provides high image fitting precision and stable feature recognition characteristics. This allows for more accurate localization of geometric center points in images and is insensitivity to defocus. Thus, it reduces coordinate deviations caused by the complex industrial production environment [21].

However, research has shown that factors such as image noise and pixel discretization can affect the localization accuracy of image feature points under the perspective projection model [4]. When the checkerboard pattern remains parallel or perpendicular in the camera view (i.e., without rotation around the z-axis), the precision of feature point detection is relatively high. However, due to the principles of camera imaging, inclined lines can become blurred. It may lead to a decrease in accuracy in detecting checkerboard corner points, which in turn reduces camera calibration precision. The accuracy and stability of control point extraction are severely affected. Furthermore, when the target plane is not parallel to the image plane, or when the center of a circle deviates from the main orientation of the vision system, the circle in the target plane may be projected as an ellipse. It will result in an eccentricity error between the actual projected center coordinates and the theoretical center coordinates of the circle [22]. Given the characteristics of large fields of view and shallow depths of field in visual systems used in industrial settings, the influence of eccentricity errors in extracting the center points of concentric circle images on camera calibration cannot be ignored. Thus, it is essential to correct and compensate for these errors.

Moreover, the essence of camera calibration is to compute the homography transformation matrix between the image plane and the calibration template plane. Therefore, the control points on the calibration template should theoretically remain on the same plane [3]. That means it requires planarity. However, in practical industrial applications, due to both the need for calibration maintenance in the production environment after the visual system is installed and the necessity of using larger calibration templates to improve maintenance efficiency under a large field of view, calibration methods must be more adaptable and robust to geometric changes, such as deformations of the calibration board, to suit real-world applications.

In summary, compared to the application of visual measurement systems in laboratories, inspection rooms, or standardized assembly lines, the application in industrial production settings faces more complex challenges, including interference from varying environmental lighting, larger measurement ranges, and higher demands for relative measurement accuracy. Undoubtedly, they pose greater challenges to camera calibration technology. Therefore, this paper proposes a

camera calibration method based on eccentricity error compensation for concentric circles and scene topological structure constraints, aiming to enhance the reliability of visual inspection in complex industrial environments and to expand the application field of visual measurement. The main contributions of this paper are as follows:

- To address issues such as variable lighting and imaging blur in industrial environments, we propose a fast detection method for concentric circle targets based on Yolov8-OBB. By employing a rotating bounding box strategy, the detection accuracy and robustness under complex lighting conditions are improved.
- To mitigate the significant eccentricity error of concentric circle targets under shallow depth-of-field conditions, we developed an iterative refinement technique based on an eccentricity error compensation method for concentric circle center points. By optimizing the homography relationship, this approach iteratively corrects perspective deviations, effectively eliminating the impact of camera distortion and ellipse center eccentricity errors on control point fitting accuracy.
- In response to geometric structural deviations caused by calibration target deformation, we introduce geometric topology constraints to accurately reconstruct the 3D structure of the calibration target. By embedding these constraints into a nonlinear optimization framework, the camera intrinsic parameters and 3D geometry are jointly optimized, enabling high-precision calibration.

2. Camera calibration algorithm based on eccentricity error compensation of concentric circles and scene topological structure constraints

Large fields of view, shallow depths of field, and geometric structural deviations of calibration boards pose significant challenges in complex industrial camera calibration scenarios. This paper introduces a novel camera calibration algorithm that utilizes eccentricity error compensation for concentric circles and fixed topological relationship constraints within the scene structure of the calibration board. The proposed method employs a calibration board with concentric circle patterns for visual camera calibration. The distinctive double-ellipse geometry of the concentric circle pattern ensures stable performance across various angles and distances while maintaining high detection and recognition accuracy under industrial conditions.

Rapid detection of concentric circle targets under complex lighting conditions is another critical problem addressed in this study. A target detection method, based on the Yolov8 Oriented Bounding Box (Yolov8-OBB), is proposed to enhance robustness and accuracy. By improving the bounding box regression mechanism of the Yolov8 model and adopting a rotating bounding box strategy, the method significantly enhances the detection accuracy and robustness of concentric circle targets in complex lighting environments. To mitigate the significant impact of eccentricity errors in concentric circle patterns on calibration in shallow depth of field visual systems, this paper employs an iterative method to optimize and compensate for the perspective deviations of the concentric circle target centers based on the homography relationship of the calibration board plane. This results in more accurate pixel coordinates for control points. Furthermore, during the overall optimization of camera calibration, the precise three-dimensional geometric shape of the calibration target is constructed based on the geometric topological constraints of the calibration board targets. Ultimately, the three-dimensional coordinate deviations of the calibration board target feature points and the eccentricity error compensation of the concentric circle feature points are optimized together with the camera's intrinsic parameters and the three-dimensional structure of the feature points through nonlinear optimization, achieving accurate camera calibration. The system flowchart is shown in Fig. 1.

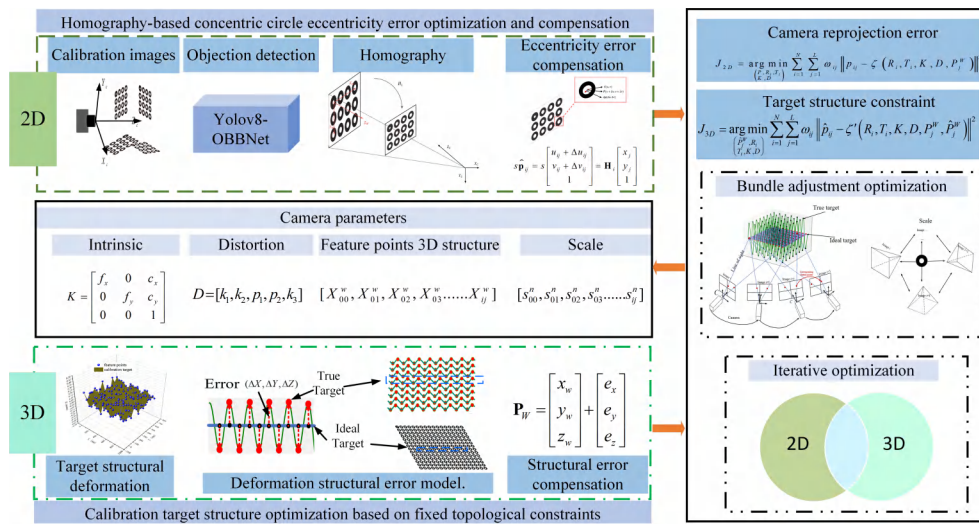


Fig. 1. Flowchart of the camera calibration algorithm.

3. Core components of the calibration algorithm

3.1. Mathematical model of the perspective eccentricity error of concentric circles

In complex industrial production environments, the camera calibration process encounters challenges such as significant variations in ambient lighting and deformation of the calibration target itself. Wide fields of view, shallow depths of field, and surface contamination of the calibration target. These factors may lead to issues like defocus and motion blur in captured images, affecting the accurate extraction of control points from calibration templates and further affecting the precision of the calibration parameters. As shown in Fig. 2, due to focusing issues, the elliptical shapes in the images captured by the camera may appear blurred. Compared to traditional checkerboard patterns, circular and concentric circle patterns, owing to their inherent

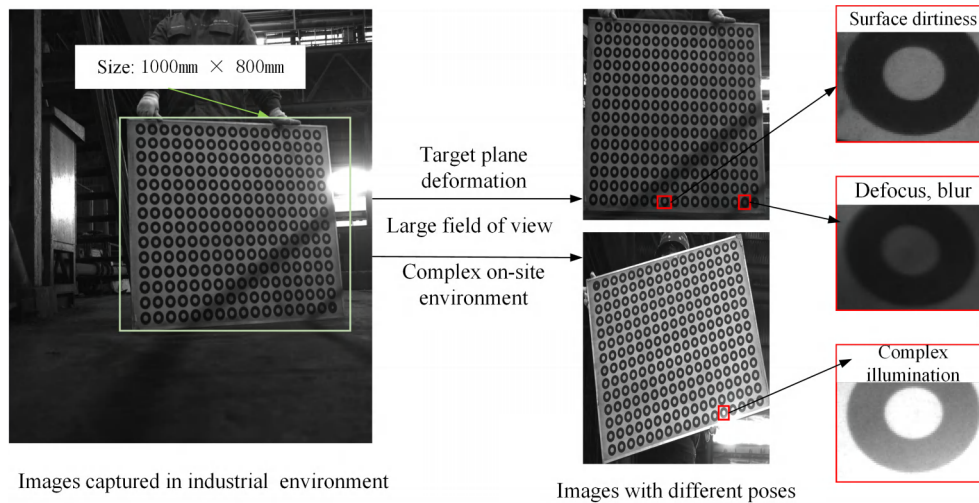


Fig. 2. Characteristics of calibration patterns acquired in industrial environments.

symmetry and consistency, can ensure high-precision detection and positioning even under conditions of a wide field of view and shallow depth of field. These patterns demonstrate stronger robustness against issues such as image defocus, blur, deformation and noise.

To achieve rapid and accurate extraction of target patterns in industrial scenarios, this study employs the Yolov8 [23] object detection model, as shown in Fig. 3. The model integrates the state-of-the-art (SOTA) architecture, with its backbone network and Neck section drawing inspiration from the design principles of Yolov7 ELAN [24]. Specifically, the model optimizes the C3 structure of Yolov5 [25] into a C2F structure and dynamically adjusts the number of channels based on the model scale. These enhancements significantly improve the model's performance. To address the issue of ellipses potentially degenerating into ellipses during imaging and the associated detection challenges, this study innovatively introduces the Yolov8-OBB technique. Compared to traditional horizontal detection algorithms, OBB not only predicts the center coordinates, width, and height of the detection box but also introduces an additional angle parameter. By utilizing the coordinates of the four endpoints of the detection box, it precisely locates the region of interest for the target. With its enhanced expressive capability of OBB, it can flexibly adapt to directional changes in target objects, thereby enabling more accurate extraction of target pattern regions on the calibration board.

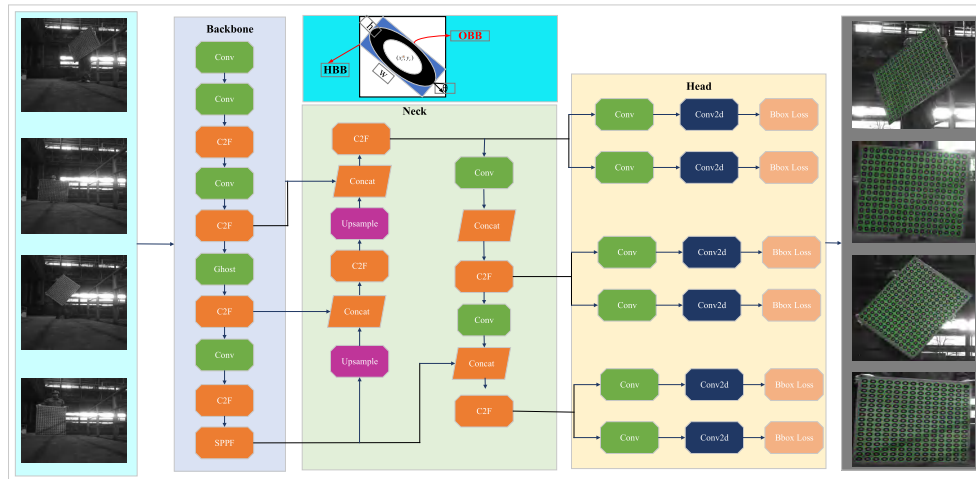


Fig. 3. Target object detection network model based on Yolov8-OBB.

The results demonstrate that the method combining Yolov8 with OBB technology not only enables rapid and precise target detection in complex industrial environments but also significantly improves the accuracy of image recognition. This method effectively reduces detection errors, enhances the robustness of image recognition in system calibration, and provides reliable technical support for industrial camera calibration.

Therefore, the overall extraction process of the subpixel center points for concentric circle targets is illustrated in Fig. 4. First, the region of interest of the target is extracted using the Yolov8-OBB network. Next, fronto-parallel transformation and subpixel edge detection are performed on the concentric circles within the region of interest. Finally, based on the common self-polar triangle property of the concentric circles, the subpixel center point coordinates of the target are calculated and determined.

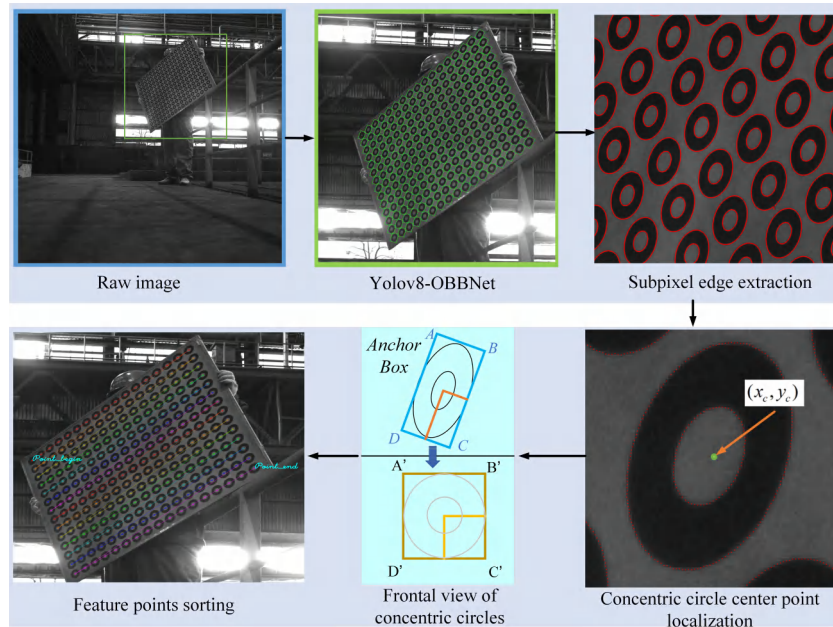


Fig. 4. Subpixel center point extraction process for concentric circle targets.

3.2. Concentric circle eccentricity error model

In the perspective projection model, when the target plane is not parallel to the image plane, the circle in the target plane is imaged as an ellipse, as shown in Fig. 5. In real cameras, lens distortion affects the image, resulting in the ellipse appearing distorted. This leads to a discrepancy between the center of the ellipse after image distortion correction and the true projected center of the circle. This is known as the eccentricity error in the localization of the circle's center during the perspective projection process. Figure 5 illustrates the eccentricity error in the aforementioned concentric circle target, where C represents the true projected center of the concentric circles, C_{in} is the center of the inner ellipse, and C_{out} is the center of the outer ellipse. C is the center of the true projected point coordinates of the concentric circles on the image plane. P is the center coordinates of the concentric circles on the image plane obtained from the coordinates of the inner and outer ellipse centers. According to the principles of photographic geometry, there will always be a certain deviation between C and P , and the offset $\Delta p = |C - P|$ is the eccentricity error.

The perspective deviation of the concentric circle center projection is given by:

$$\Delta p = |C - P| \quad (1)$$

3.3. Optimization compensation for eccentricity error of concentric circles based on planar homography

The actual projected center coordinates of the concentric circles play a critical role in camera calibration, as they directly affect the determination of camera parameters. Therefore, accurately solving for the true pixel coordinates of the centers of the concentric circle is particularly important. Most of the existing studies have addressed the eccentricity error by constructing a mathematical model for the projection of concentric circles and performing a one-time perspective geometric compensation. Although this method is theoretically feasible, it is computationally

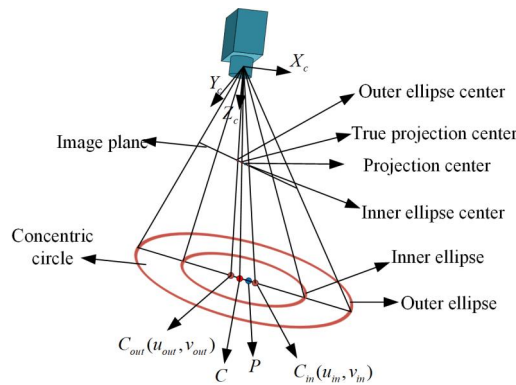


Fig. 5. Projection of concentric circles in the perspective model and real camera model.

complex. Thus, it is not widely applicable in practical scenarios. In projective geometry, the linear projection transformation between the calibration board plane target and the image plane is referred to as a homography relationship, as illustrated in Fig. 6. In Fig. 6(a), $O_X_WY_WZ_W$ represents the world coordinate system of the calibration board, while $O_X_CY_CZ_C$ denotes the camera coordinate system. The matrix H_i is the homography matrix between the calibration board plane and its image plane, which can be derived from the centers of the concentric ellipses and their corresponding world coordinates. Since the calibration board plane is the XOY plane, the Z -coordinate of the feature points on the standard calibration board plane is 0. The undistorted image feature homogeneous coordinates of the feature point $q_j = [x_j, y_j, 0, 1]^T$ on the calibration board plane at the $i - th$ row and $j - th$ column is denoted as $p_{ij} = [u_{ij}, v_{ij}, 1]^T$. Under ideal conditions, the correspondence between p_{ij} and q_j can be expressed through their homography as follows:

$$s \begin{bmatrix} u_{ij} \\ v_{ij} \\ 1 \end{bmatrix} = H_i \begin{bmatrix} x_j \\ y_j \\ 0 \\ 1 \end{bmatrix} \quad (2)$$

where s is a scale factor.

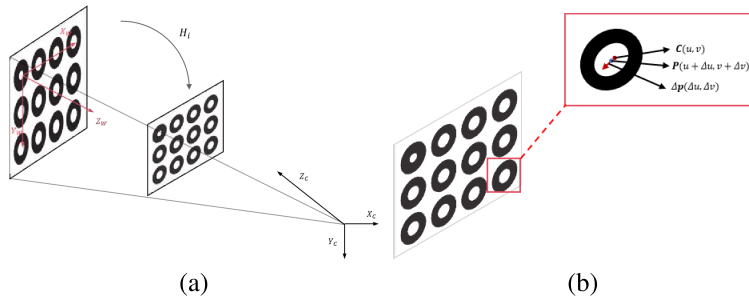


Fig. 6. Homography relationship between the concentric circle calibration target and the image plane. (a) Homography between the concentric circle calibration target and the image plane; (b) Optimization of concentric circle eccentricity error.

Based on the homography relationship between the image plane and the calibration board plane, optimizing eccentricity error compensation for the concentric circle projection center can be achieved by minimizing the reprojection error. As shown in Fig. 6(b), the blue point P represents the initial coordinates of the image feature point, while the red point C is the image coordinate $\hat{\mathbf{p}}_{ij} = [u_{ij} + \Delta u_{ij}, v_{ij} + \Delta v_{ij}, 1]^T$ after eliminating the eccentricity error. The relationship between $\hat{\mathbf{p}}_{ij} = [u_{ij} + \Delta u_{ij}, v_{ij} + \Delta v_{ij}, 1]^T$ and q_{ij} can be expressed as:

$$s\hat{\mathbf{p}}_{ij} = s \begin{bmatrix} u_{ij} + \Delta u_{ij} \\ v_{ij} + \Delta v_{ij} \\ 1 \end{bmatrix} = \mathbf{H}_i \begin{bmatrix} x_{ij} \\ y_{ij} \\ 1 \end{bmatrix} \quad (3)$$

Nonlinear optimization is employed to adjust for the eccentricity error and minimize the reprojection error. The reprojection error is defined as:

$$E = \sum_i \left\| \begin{bmatrix} u_{ij} \\ v_{ij} \end{bmatrix} - \begin{bmatrix} u'_{ij} \\ v'_{ij} \end{bmatrix} \right\|^2 \quad (4)$$

where (u'_{ij}, v'_{ij}) is the pixel coordinate computed through the corrected homography relationship.

Under this assumption, a target function for minimizing the reprojection error of the target feature points in the image is established, as shown in Eq. (5):

$$J_{2D} = \arg \min_{\begin{pmatrix} P, R_i, T_i \\ K, D \end{pmatrix}} \sum_{i=1}^N \sum_{j=1}^L \omega_{ij} \|p_{ij} - \zeta(R_i, T_i, K, D, P_j^W)\|^2 \quad (5)$$

where N is the total number of images, L is the total number of feature points on the calibration template, ω_{ij} takes values of 0 or 1 to indicate whether this feature point was collected in the image, p_{ij} is the image coordinate of the j -th feature point at position i , R_i, T_i, K, D represents the camera's intrinsic and extrinsic parameters, P_j^W denotes the three-dimensional coordinates of the feature points on the standard plane, P represents the set of two-dimensional coordinate points of the feature points, and the function $\zeta(\bullet)$ represents the reprojection process of feature points from world coordinates to image coordinates. By utilizing the Levenberg-Marquardt algorithm to optimize Eq. (5), the optimized image feature points \hat{p}_{ij} can be obtained.

3.4. Deformation error model and optimization of calibration target based on fixed topological relationship constraints

In visual measurement systems within complex industrial environments, calibration boards may deform over prolonged use due to factors such as handling, collisions, and variations in environmental temperature and humidity. These deformations can cause deviations in the three-dimensional coordinates of the feature points on the calibration board. And this will affect the calibration accuracy and negatively impact the measurement results of the industrial measurement system.

The deformation parameters of feature points on the calibration board can be represented by the three-dimensional deviation factors of each point. Let the ideal three-dimensional coordinates of the feature points on the calibration board be $P_j^W = (X_j, Y_j, Z_j)$, and the actual coordinates considering deformation errors be $\hat{P}_j^W = (X'_j, Y'_j, Z'_j)$, as shown in Fig. 7. The deviation factors

for each coordinate component follow a Gaussian distribution $\mathcal{N}(0, \sigma^2)$. Therefore, the actual coordinates of the feature points can be expressed as:

$$\begin{aligned} X'_j &= X_j + \Delta X_j, \quad \Delta X_j \sim \mathcal{N}(0, \sigma_X^2) \\ Y'_j &= Y_j + \Delta Y_j, \quad \Delta Y_j \sim \mathcal{N}(0, \sigma_Y^2) \\ Z'_j &= Z_j + \Delta Z_j, \quad \Delta Z_j \sim \mathcal{N}(0, \sigma_Z^2) \end{aligned} \quad (6)$$

where $\varepsilon_j = (\Delta X_j, \Delta Y_j, \Delta Z_j)$ represents the deformation errors of the feature point coordinates P_j^W .

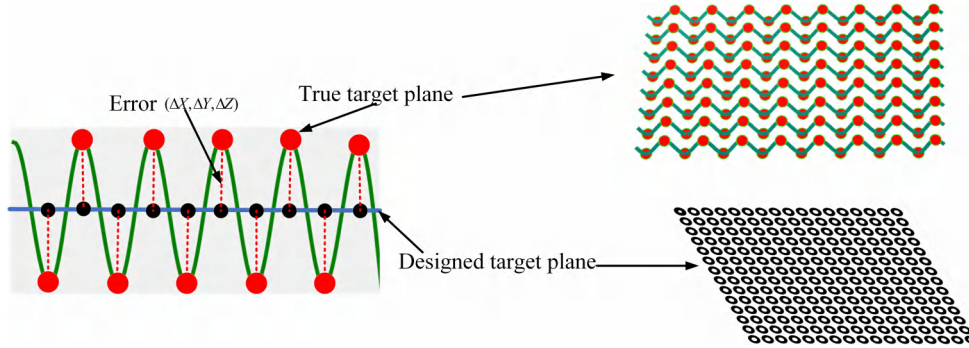


Fig. 7. Standard plane of the calibration board and the deformed plane.

Traditional Zhang's calibration method assumes that the three-dimensional coordinates of the feature points lie on the same plane (usually $Z = 0$), thus establishing the correspondence between the image and the actual space by calculating the homography matrix. However, when the calibration board experiences deformation, the feature points no longer satisfy the plane assumption. The deformation errors can propagate through subsequent nonlinear optimization to the optimization variables, including both intrinsic and extrinsic camera parameters. So, the accuracy of camera calibration may reduce. Additionally, directly using the initial three-dimensional coordinates of the calibration target control points as optimization targets can lead to excessive optimization parameters during nonlinear optimization, causing instability. Therefore, this paper employs a multi-view geometric approach to obtain the three-dimensional coordinates of the feature points on the deformed calibration board. For the collected images of the geometrically deformed calibration board, the bundle adjustment method is used to calculate the three-dimensional coordinates of the target feature points in order to obtain the structure of the planar scene.

During the camera calibration process, multiple observations of the feature points on the calibration board are made. Then the least squares method is employed to estimate the camera's intrinsic and extrinsic parameters. Let the true three-dimensional coordinates of the calibration board be P_{ij} , and the corresponding pixel coordinates be $p_{ij} = (u_{ij}, v_{ij})$. According to the camera model, the process of mapping these three-dimensional points onto the image plane can be represented by Eq. (7):

$$s \begin{bmatrix} u_{ij} \\ v_{ij} \\ 1 \end{bmatrix} = K[R \mid T] \left(\begin{bmatrix} X_{ij} \\ Y_{ij} \\ Z_{ij} \end{bmatrix} + \begin{bmatrix} \Delta X_{ij} \\ \Delta Y_{ij} \\ \Delta Z_{ij} \end{bmatrix} \right) = K[R \mid T] \begin{bmatrix} X'_{ij} \\ Y'_{ij} \\ Z'_{ij} \\ 1 \end{bmatrix} \quad (7)$$

where s is the scale factor, K is the camera's intrinsic parameters, R is the rotation matrix, and T is the translation vector. To minimize the reprojection error E , the Levenberg-Marquardt algorithm is applied to Eq. (8):

$$\min_{(\Delta u_{ij}, \Delta v_{ij}), (\Delta X_{ij}, \Delta Y_{ij}, \Delta Z_{ij})} \sum_i \left\| \begin{bmatrix} u_{ij} + \Delta u_{ij} \\ v_{ij} + \Delta v_{ij} \\ 1 \end{bmatrix} - \frac{1}{s} K[R | T] \begin{bmatrix} X_{ij} + \Delta X_{ij} \\ Y_{ij} + \Delta Y_{ij} \\ Z_{ij} + \Delta Z_{ij} \\ 1 \end{bmatrix} \right\| \quad (8)$$

Then the optimal estimates of the deformation deviation $(\Delta X_{ij}, \Delta Y_{ij}, \Delta Z_{ij})$ and eccentricity error compensation $(\Delta u_{ij}, \Delta v_{ij})$ can be obtained.

3.5. Optimization of bundle adjustment based on multi-View collinearity equations

The purpose of bundle adjustment is to minimize the sum of the squared reprojection errors between the reprojected image points of all world coordinate points across multiple images (as shown in Fig. 8(a): Image $i, \dots, i+1, i+2, i+3$) and their actual projections. This minimization of reprojection error aims to optimize the world coordinates of the feature points on the calibration board, resulting in more accurate world coordinates for the feature points. The bundle adjustment method uses collinearity equations as a mathematical model. The pixel coordinates of the two-dimensional imaging points of the calibration template control points are nonlinear functions of the camera's intrinsic and extrinsic parameters and the three-dimensional coordinates of the control points. After linearization, calculations are performed according to the principles of least squares. Finally, the optimal value is approached iteratively.

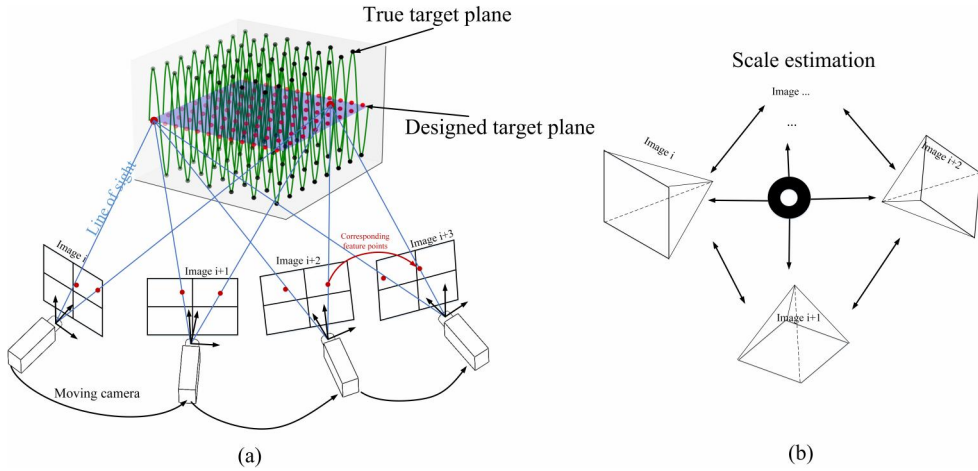


Fig. 8. Multi-view geometric measurement method of bundle adjustment.

In the world coordinate system, the coordinates of the camera center C is (X_0, Y_0, Z_0) . The coordinates of a point P in space in the world coordinate system is (X_p, Y_p, Z_p) . The pixel image point on the image of P and its auxiliary coordinates in the image plane and image space is $(x_p, y_p, -f)$. It is known that the points C, p, P are collinear. Thus, we can derive:

$$\frac{X_p}{X - X_0} = \frac{Y_p}{Y - Y_0} = \frac{Z_p}{Z - Z_0} \quad (9)$$

The collinearity equation can be expressed as:

$$\begin{cases} x_p = x_0 + \Delta x - f \frac{m_{11}(X_p - X_0) + m_{12}(Y_p - Y_0) + m_{13}(Z_p - Z_0)}{m_{31}(X_p - X_0) + m_{32}(Y_p - Y_0) + m_{33}(Z_p - Z_0)} \\ y_p = y_0 + \Delta y - f \frac{m_{21}(X_p - X_0) + m_{22}(Y_p - Y_0) + m_{23}(Z_p - Z_0)}{m_{31}(X_p - X_0) + m_{32}(Y_p - Y_0) + m_{33}(Z_p - Z_0)} \end{cases} \quad (10)$$

where (m_{11}, \dots, m_{33}) is the rotation matrix coefficient for each camera relative to the world coordinate system, and Δx and Δy represent positional offsets caused by radial distortions (including distortion coefficients k_1, k_2, k_3) and tangential distortions (including coefficients p_1, p_2).

Using the multi-view geometric measurement method of bundle adjustment, the true three-dimensional coordinates of all control points on the calibration board, namely, the centers of the concentric circles, are obtained. Then, these three-dimensional coordinates are associated with the iteratively compensated image feature points to establish the correspondence. Finally, the objective function can be formed based on minimizing the reprojection error :

$$J_{3D} = \arg \min_{\begin{pmatrix} \hat{P}_j^W, R_i \\ T_i, K, D \end{pmatrix}} \sum_{i=1}^N \sum_{j=1}^L \omega_{ij} \left\| \hat{p}_{ij} - \zeta' \left(R_i, T_i, K, D, P_j^W, \hat{P}_j^W \right) \right\|^2 \quad (11)$$

where \hat{p}_{ij} represents the image coordinates of the j -th feature point at position i after iterative compensation. Meanwhile, the geometric topological structure of the calibration board is used as a constraint in the nonlinear optimization process when optimizing the world coordinates of the feature points. The Levenberg-Marquardt algorithm from the Ceres Solver library [26] is employed to yield optimal solutions for the camera's intrinsic and extrinsic parameters as well as the three-dimensional coordinates of the calibration template feature points.

In the camera calibration process, the scale factor is calculated based on the dimensional information of the concentric circle target and applied to the calibration process, as illustrated in Fig. 8(b). Through the above optimization process, the bundle adjustment optimization based on collinearity equations can effectively adjust the camera parameters and three-dimensional point coordinates. Thus, the topological structural relationships of the deformed calibration board can be ensured. This process is achieved through iterative optimization of the bundle adjustment method, resulting in more accurate final three-dimensional point coordinates and camera parameters that conform to the actual geometric topological structure.

3.6. Iterative optimization method for camera calibration

After optimizing the compensation for the perspective deviation of the projection centers of concentric circle and the three-dimensional coordinates of feature points on the calibration board, further optimization of the camera intrinsic parameters and distortion parameters was conducted. Through this optimization, it is possible to accurately compute the camera's perspective projection parameter matrix and distortion coefficient matrix. To further improve the accuracy of the camera parameters, this paper employs an iterative method to meticulously adjust and optimize these parameters, thereby obtaining more precise and stable camera parameters. It can provide a reliable foundation for subsequent visual measurement and three-dimensional reconstruction.

Considering the radial and tangential distortion of the camera lens, the Brown-Conrady lens distortion model is used. The real observed image coordinates resulting from lens distortion can be modeled as:

$$\begin{bmatrix} x_d \\ y_d \end{bmatrix} = (1 + k_1 r^2 + k_2 r^4 + k_3 r^6) \begin{bmatrix} x_c \\ y_c \end{bmatrix} + \begin{bmatrix} 2p_1 x_u y_u + p_2(r^2 + 2x_u^2) \\ p_1(r^2 + 2y_u^2) + 2p_2 x_u y_u \end{bmatrix} \quad (12)$$

where (x_c, y_c) represents the coordinates of a point in the undistorted image physical coordinate system, and (x_d, y_d) represents its corresponding distorted coordinates. r is the distance from the point to the distortion center, defined as $r^2 = x_u^2 + y_u^2$. $(k_1, k_2, k_3, p_1, p_2)$ are the distortion coefficients of the lens, where k_1, k_2 and k_3 are the radial distortion coefficients, and p_1, p_2 are the tangential distortion coefficients.

This paper uses the bundle adjustment method to minimize the reprojection error of all frames, determining all camera parameters (including the relative positions of all calibration targets, camera poses, and intrinsic parameters). The cost function is expressed as follows:

$$f(x, P, K, D, R, T) = \arg \min(J_{2D} + J_{3D}) \quad (13)$$

where x represents the feature point pixel coordinates, and P represents the world three-dimensional coordinates of the feature points. This results in the optimized camera intrinsic and extrinsic parameters, along with the corresponding pixel coordinates in the original image and the three-dimensional coordinates of the feature points.

4. Experimental results and analysis

To validate the effectiveness of the proposed method, this section conducts detailed performance evaluations through both simulated and real experiments. And we compared the proposed method with the camera calibration methods proposed by Zhang [2], Liu [4], Strobl [6] and Song [5]. In the experiments, the method is evaluated for its accuracy and robustness in terms of camera intrinsic parameters, system reprojection error, and geometric accuracy of the calibration target under different experiments. In addition, in real experiments, different methods are applied to the constructed stereo vision system to compare their accuracy in measuring baseline distances.

4.1. Experimental results and analysis

The system simulation was conducted with a camera resolution of 5120×5120 pixels. The pixel size is 2.5 micrometers, and the lens focal length is set to 12 mm. The calibration target used was a concentric circle plane target with 17×14 control points. The distance between adjacent concentric circle control points is 55.0 mm. The diameter of the outer circle is 46 mm and the inner one is 20 mm. And the inner diameter of the positioning circle is 10 mm, as shown in Fig. 9. All images were captured randomly within the following parameter ranges: the distance from the target plane to the camera was between 1500 and 2000 mm, and the angle between the target plane and the image plane was from 0 to 60 degrees. The root mean square errors (RMSE) of the reprojection error between the camera parameters and the feature points on the image plane, as well as the geometric structure deviation errors of the calibration board, are used as performance metrics to compare with the camera calibration methods of Zhang [2], Liu [4], Strobl [6] and Song [5].

4.2. Experimental results and analysis

This section provides a comprehensive validation of the proposed method through detailed monocular camera calibration experiments and stereo vision measurement experiments. The monocular camera calibration experiment involved the calibration of images captured by a multi-line structured light measurement system for corner edge measurement of continuously cast slabs in an industrial setting. The measurement system features a large field of view and shallow depth of field. It is located in an open environment within a factory, characterized by complex lighting conditions, including both natural and artificial light sources, with unstable light intensity and direction. The calibration board surface is made of aluminum oxide, with a pattern size of 926×761 mm and an initial processing accuracy of 0.01 mm, while the calibration board itself has undergone approximately 1 mm of deformation. The stereo vision measurement

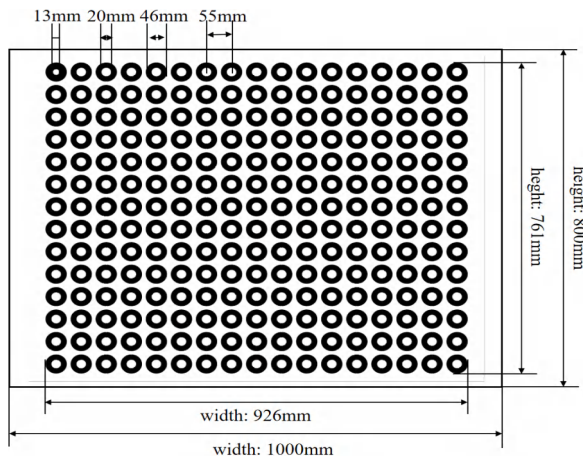


Fig. 9. Calibration target.

system experiment was conducted in a laboratory, featuring similar characteristics of a large field of view and shallow depth of field. During the experiment, the camera's exposure time and laboratory lighting were controlled to mimic the lighting conditions in the industrial environment. Through these two experiments, the stability and accuracy of the proposed camera calibration method in complex environments are demonstrated.

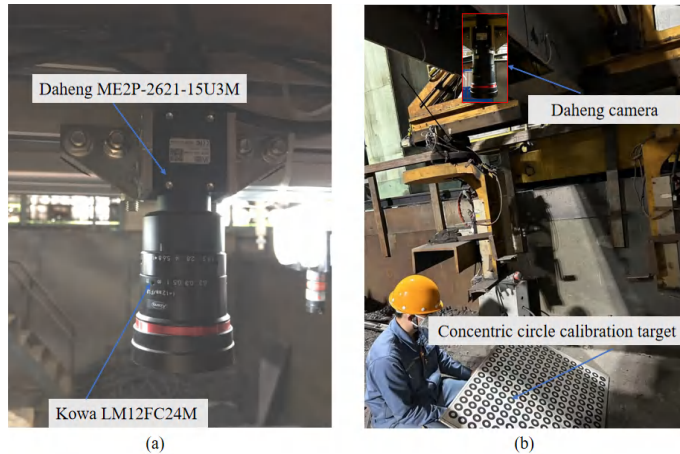


Fig. 10. Camera calibration in industrial production environment. (a) Monocular camera system; (b) On-site calibration operations.

4.3. Monocular camera calibration validation experiment

In addition to simulation experiments, this paper also conducted field experiments for the calibration of monocular vision and investigated the practical efficiency of the proposed camera calibration method. The configuration of the monocular vision imaging system used in the tests is shown in Fig. 10(a), using an industrial camera (Daheng Imaging, ME2P-2621-15U3M) with a resolution of 5120×5120 pixels and a focal length of 12 mm (Kowa, LM12FC24M). Figure 10(b) shows the scene of the monocular camera calibration.

The experiment selected two different monocular vision imaging systems to perform field calibration using the same calibration board. During the camera calibration process, the calibration board target of every monocular system was placed in 35 different positions. Figure 11(a-e) shows a selection of images collected by the system. A comparative analysis was performed with the calibration results obtained from the proposed method and those from Zhang's, Liu's, Strobl's, and Song's methods. We compared the reprojection errors of target feature points and the geometric analysis of the calibration board to verify the effectiveness of the proposed method. The calibration results of the camera parameters from the images collected by the system obtained from the five methods are shown in Table 1. The uncertainty U_{f_x} , U_{f_y} , U_{u_0} , U_{v_0} , U_{k_1} , U_{k_2} , U_{p_1} , U_{p_2} , U_{k_3} of the calibration parameter $f_x, f_y, u_0, v_0, k_1, k_2, p_1, p_2, k_3$ is shown in Table 2. It indicates that the uncertainty of the camera parameters obtained by the proposed method is significantly lower than that of Zhang's, Liu's, and Song's methods. Compared to Zhang's method, the uncertainties of f_x, f_y and k_1, k_2 are reduced by three times, while the uncertainties of the principal point's coordinates are reduced by 4 to 6 times. The proposed method also outperforms Strobl's method.

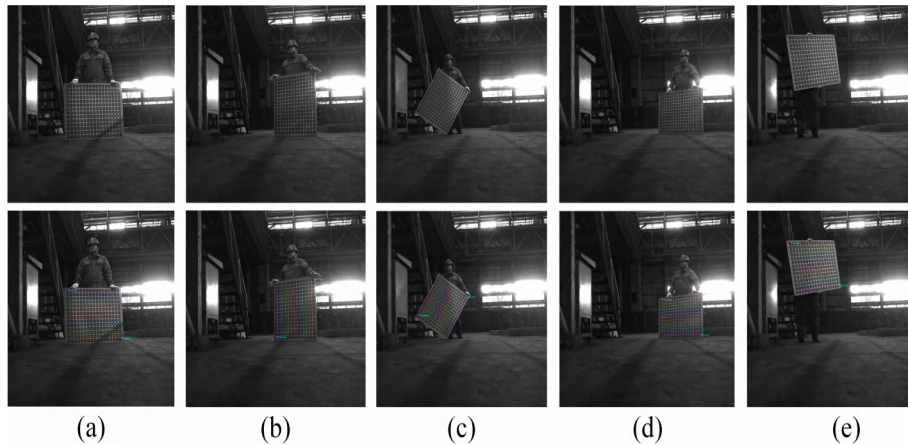


Fig. 11. Calibration images collected by the monocular vision system.

Table 1. Camera intrinsic parameters obtained by different methods

	f_x	f_y	u_0	v_0	k_1	k_2	p_1	p_2	k_3	RMS
Zhang's	4937.13	4937.02	2525.06	2588.56	-0.065	0.154	5.62e-4	-3.34e-4	-3.03e-2	0.36
Liu's	4926.75	4926.65	2885.36	2609.81	-0.068	0.153	4.21e-04	2.95e-04	-4.72e-02	0.26
Strobl's	4925.25	4925.56	2542.14	2658.04	-0.068	0.145	4.83e-04	-1.94e-04	-2.62e-02	0.11
Song's	4930.21	4930.23	2521.42	2636.52	-0.069	0.152	8.54e-04	-1.03e-04	-4.35e-02	0.18
Proposed	4927.65	4927.55	2573.08	2594.21	-0.066	0.144	1.13e-4	-3.15e-4	-3.65e-2	0.07

From the data in Table 1, it is evident that the uncertainties of the parameters obtained by the proposed camera calibration method are significantly better than those of Zhang's method. And the uncertainty for f_x, f_y and k_1, k_2 is reduced by twice. Additionally, the uncertainty of the principal point's coordinates obtained by the proposed method is about four times lower compared to Zhang's method. The uncertainty of the tangential distortion parameters is also slightly better than that of Zhang's method.

Table 1 shows the RMS values of the reprojection errors of the target feature points using Zhang's, Liu's, Strobl's, and Song's methods, respectively. From Table 1, it can be observed that

Table 2. Comparison results of uncertainty in camera intrinsic parameters

	U_{fx}	U_{fy}	U_{u_0}	U_{v_0}	U_{k_1}	U_{k_2}	U_{p_1}	U_{p_2}	U_{k_3}
Zhang's	9.56	9.81	0.51	0.49	0.009	0.068	0.0016	0.0005	0.013
Liu's	2.78	2.89	0.86	0.84	0.032	0.046	0.0007	0.0006	0.009
Strobl's	1.23	1.36	0.45	0.49	0.007	0.032	0.0006	0.0005	0.006
Song's	2.36	3.45	0.36	0.38	0.021	0.039	0.0008	0.0007	0.004
Proposed	0.56	0.64	0.22	0.31	0.005	0.013	0.0002	0.0005	0.002

the average reprojection error based on the proposed method is 0.07 pixels, while the average reprojection errors based on Zhang's, Liu's, Strobl's, and Song's methods are 0.36, 0.26, 0.11, and 0.18 pixels. The scatter plot also shows that the proposed method not only accurately recovers the calibration parameters but is also stable because the scatter points are symmetrically distributed around the origin. These figures indicate that the reprojection error distribution of the target feature points from the proposed method is significantly better than that of the comparison methods. Figure 12(a) illustrates the variation of the average reprojection error with increasing iteration counts. Figure 12(b) shows the final geometric structure of the calibration board obtained using the proposed method. Ten repeatability measurement experiments were conducted for this monocular system, using the proposed method and Strobl's method. And the measurement results for the geometric structure deviation of the calibration target. Experimental results show that our method significantly outperforms the Strobl method in terms of RMS error, maximum error, and average error. The root mean square error of our method is 0.007 mm, a decrease of 87.6% compared to the Strobl method's 0.0563 mm. The RMS error decreases from 0.024 mm to 0.01 mm, a decrease of 58.3%. The maximum reconstruction error decreases from 0.0756 mm to 0.0514 mm, a decrease of 32.0%. Therefore, it can be concluded that the proposed camera calibration method, based on compensating for the eccentricity error of the concentric circles and constraining the scene's topological structure, can more accurately and stably reconstruct the geometric shape of the calibration board during the camera calibration process. The results demonstrate that the proposed method reduces the reprojection error of the target feature points when using calibration boards with geometric deformation, significantly improving the calibration accuracy of the visual system.

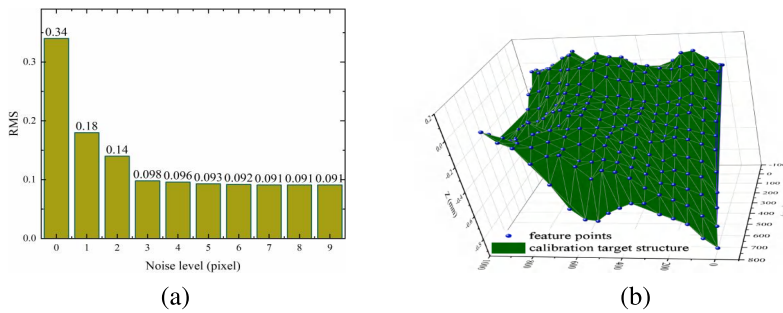


Fig. 12. (a) Relationship between camera calibration reprojection error and iteration count;
(b) Reconstructed target structure of the calibration target.

4.4. Binocular vision system validation experiment

To further validate the effectiveness of the proposed calibration method, an experiment was conducted using a binocular vision imaging system. The experimental setup involved securing the binocular camera system on a tripod to ensure stability and alignment with the test area, as

illustrated in Fig. 13. The system employs a Daheng Imaging ME2P-2621-15U3M industrial camera, featuring a resolution of 5120×5120 pixels and a pixel size of 2.5 microns, together with a Kowa LM12FC24M 12 mm lens. To achieve an adequate depth of field for measurements, the lens aperture was set to $F = 8.0$. The image capture area was positioned at a distance of 1.5 to 2.0 meters from the camera. The maximum deformation of the concentric circle calibration board used for the system calibration was 1.0 mm.

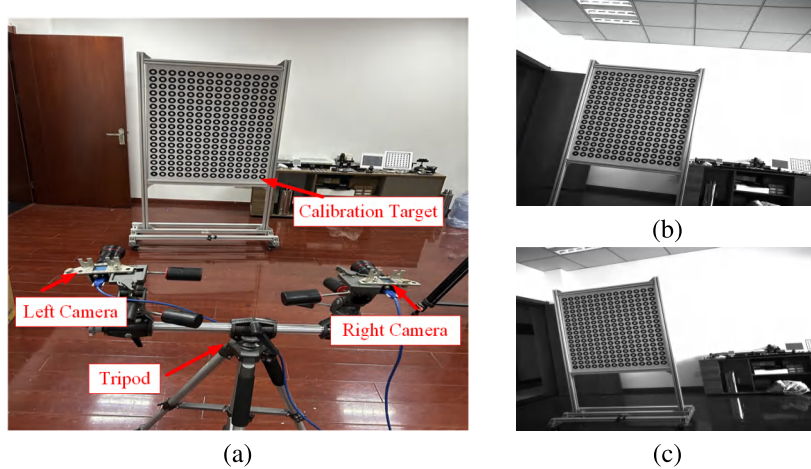


Fig. 13. Binocular vision system and some collected calibration patterns.

In this study, the Euclidean distance between the provided global coordinates M and the reconstructed global coordinates \hat{M} obtained from the binocular vision imaging system was used as a criterion to evaluate the accuracy of the measurement system:

$$E_{\text{pt}} = \frac{1}{n} \sum_{i=1}^n \sqrt{\|M_i - \hat{M}_i\|^2} \quad (14)$$

where n is the number of measurements.

In the experiment, the proposed method was initially applied to accurately calibrate the binocular vision imaging system. 35 sets of calibration images were captured, a selection of which is shown in Fig. 13(b) and (c). The internal and external camera parameters were calculated using the Zhang's, Liu's, Strobl's, and Song's camera calibration methods, along with the proposed method. The results are presented in Table 3. The baseline images captured by the binocular vision imaging system were then used to verify the accuracy of the calibration parameters. The baseline ruler is 960.98 mm in length. Figure 14 shows a pair of images of the baseline ruler captured by the system. By comparing the measurement distances of the targets on the baseline ruler obtained from the binocular vision system with the actual distances, the accuracy of the calibration method was assessed. To ensure the reliability of the experimental results, the baseline ruler was measured 35 times, with variations in position and orientation. And statistical analysis was conducted. The mean, root mean square error (RMS), and maximum error (Max) of the measurement errors were calculated based on the result of the final data for analysis.

Table 3 presents the results of the calibration parameter of the binocular vision imaging system using various methods. It is evident that the reprojection error for the system calibrated using the proposed method is the smallest, followed by the Strobl's method, while the Zhang's calibration method exhibits the largest reprojection error. In monocular camera calibration, the reprojection

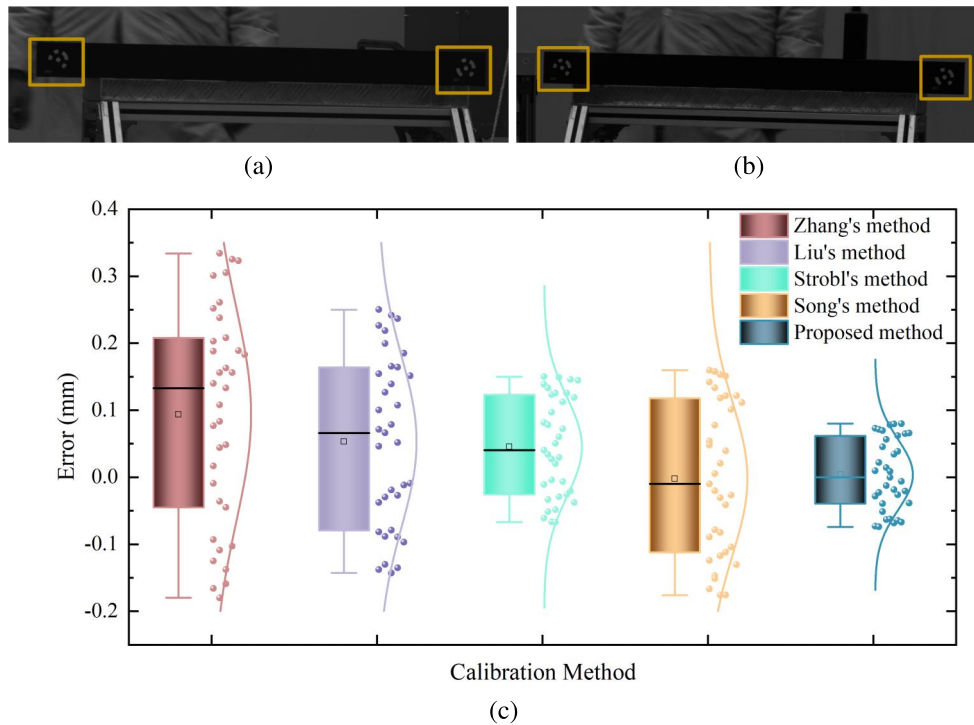


Fig. 14. Standard object patterns collected by the binocular vision imaging system and error statistics between the measured data and standard length. (a)(b) A set of standard object images simultaneously captured by the left and right cameras; (c) Measurement error distribution of the baseline ruler obtained using different calibration methods.

Table 3. Comparison of re-projection errors in binocular stereo vision systems by different methods (pixels)

Zhang's Method		Liu's Method		Strobl's Method		Song's Method		Proposed Method	
Left Cam	Right Cam	Left Cam	Right Cam	Left Cam	Right Cam	Left Cam	Right Cam	Left Cam	Right Cam
RMS	0.23	0.24	0.16	0.21	0.08	0.09	0.08	0.09	0.06
RMS	0.56		0.35		0.12		0.23		0.08

errors of the left and right cameras obtained with the Zhang's calibration method were the highest, at 0.23 and 0.24 pixels, respectively. In contrast, the proposed method achieved reprojection errors of 0.06 and 0.07 pixels for the left and right cameras, reducing the reprojection errors by 73.9% and 70.8%. The reprojection errors for the left and right cameras using the Strobl's calibration method were 0.08 and 0.09 pixels. Compared to Strobl's method, the proposed method reduced the reprojection errors by 25.0% and 22.22%. In the calibration experiment of the binocular vision system using Zhang's camera calibration method, the reprojection error was 0.56 pixels, while the proposed method achieved a reprojection error of 0.08 pixels, representing an 85.71% reduction in RMS compared to Zhang's method. Compared to Strobl's method, the proposed method achieved a 33.3% reduction in RMS for the binocular vision system. These experimental results indicate that the proposed calibration optimization method significantly improves the calibration accuracy of the binocular vision imaging system, demonstrating its effectiveness and practicality.

The measurement errors of the binocular vision imaging system are illustrated in Fig. 14. Table 4 presents the error statistics for 35 sets of baseline ruler measurement data and standard distance data. Figure 14(c) shows that the proposed method significantly reduces measurement errors and fluctuations in the results when measuring the baseline ruler. Furthermore, Table 4 indicates that the proposed method achieves the best results in terms of Mean, RMS, and Max comparisons. The average values of Mean, RMSE and Max calculated by the proposed method are 0.04 mm, 0.05 mm, and 0.08 mm. The proposed method achieves reductions of 75.0%, 72.22%, and 75.76% compared to Zhang's method. When compared to the Strobl method, reductions of 50.0%, 44.44%, and 46.67% were also observed.

Table 4. Statistical data of reference ruler length errors measured by different calibration methods (mm)

	Zhang's Method	Liu's Method	Strobl's Method	Song's Method	Proposed Method
Mean	0.16	0.11	0.08	0.10	0.04
RMSE	0.18	0.13	0.09	0.11	0.05
Max	0.33	0.25	0.15	0.18	0.08

The above analysis indicates that when using a calibration board with deformation, the proposed method results in smaller fluctuations in both intrinsic and extrinsic parameters compared to the methods of Zhang, Liu, Strobl, and Song. Additionally, the reprojection and 3D measurement errors produced by the proposed method are smaller and more stable. The results of experiments suggest that the proposed camera calibration method effectively incorporates the eccentricity errors of the concentric circle calibration points and the geometric structure information of the calibration board, significantly improving the global calibration accuracy of the measurement system. Therefore, the proposed method performs optimally in both monocular and binocular camera calibration and measurement. Strobl's method considers the three-dimensional geometric structure deformation of the calibration board used in the system, resulting in good calibration and measurement outcomes. In contrast, the methods proposed by Liu and Song focus solely on the accuracy of feature point localization, neglecting the geometric structure deformation information of the calibration board, which leads to slightly inferior results compared to the proposed method. Traditional methods, such as Zhang's method, utilize a checkerboard as the calibration board and require strict coplanarity of feature points. This requirement results in the poorest calibration and measurement outcomes when a deformed calibration board is used. This highlights the effectiveness of the proposed method in improving the measurement accuracy of the binocular system.

Based on the data analysis above, the proposed calibration method provides more stable system calibration parameters, and the calculated 3D reconstruction corner points of the baseline ruler are closer to the actual 3D distances. This not only highlights the significant impact of the calibration method on improving the performance of binocular vision imaging systems in practical applications but also demonstrates its robustness and reliability in system calibration. Consequently, the proposed method significantly enhances the measurement accuracy of the visual system.

5. Conclusion

This study presents a camera calibration algorithm based on the eccentricity error of concentric circles and the fixed topological relationship constraints of the calibration board structure, offering an effective solution for accurate calibration of visual sensors in industrial production environments. By calculating the homography relationship of the concentric circle pattern and iteratively optimizing the eccentricity error, as well as precisely locating feature points using the fixed scene topological structure constraints of the calibration board, the calibration accuracy of

the camera's internal parameters has been significantly enhanced. The results of the experiments indicate that the algorithm demonstrates good accuracy and stability when dealing with complex lighting conditions, large objects, and non-standard calibration templates. Experimental results show that the proposed calibration algorithm can effectively correct errors related to calibration board processing and geometric deformation, ensuring the accuracy of feature point locations. Compared to other calibration methods, the proposed camera calibration method exhibits greater robustness and adaptability in complex industrial environments. It provides a reliable foundation for visual measurement tasks.

Disclosures. The authors declare no conflict of interest.

Data availability. Data underlying the results presented in this paper are not publicly available at this time but may be obtained from the authors upon reasonable request.

References

1. R. Hartley and A. Zisserman, *Multiple view geometry in computer vision* (Cambridge university press, 2003).
2. Z. Zhang, "A flexible new technique for camera calibration," *IEEE Trans. Pattern Anal. Machine Intell.* **22**(11), 1330–1334 (2000).
3. A. Datta, J.-S. Kim, and T. Kanade, "Accurate camera calibration using iterative refinement of control points," in *2009 IEEE 12th International Conference on Computer Vision Workshops, ICCV Workshops*, (IEEE, 2009), pp. 1201–1208.
4. Z. Liu, Q. Wu, X. Chen, *et al.*, "High-accuracy calibration of low-cost camera using image disturbance factor," *Opt. Express* **24**(21), 24321–24336 (2016).
5. C. Song, J. Shin, M.-H. Jeon, *et al.*, "Unbiased estimator for distorted conics in camera calibration," in *Proceedings of the IEEE/CVF Conference on Computer Vision and Pattern Recognition*, (2024), pp. 373–381.
6. K. H. Strobl and G. Hirzinger, "More accurate pinhole camera calibration with imperfect planar target," in *2011 IEEE international conference on computer vision workshops (ICCV workshops)*, (IEEE, 2011), pp. 1068–1075.
7. W. Huang, H. Miao, S. Jiao, *et al.*, "A planar constraint optimization method to improve camera calibration for imperfect planar targets," *Opt. Lasers Eng.* **180**, 108273 (2024).
8. Y. Lochman, K. Liepieszov, J. Chen, *et al.*, "Babelcalib: A universal approach to calibrating central cameras," in *Proceedings of the IEEE/CVF International Conference on Computer Vision*, (2021), pp. 15253–15262.
9. T. Strauß, J. Ziegler, and J. Beck, "Calibrating multiple cameras with non-overlapping views using coded checkerboard targets," in *17th international IEEE conference on intelligent transportation systems (ITSC)*, (IEEE, 2014), pp. 2623–2628.
10. S. Peng and P. Sturm, "Calibration wizard: A guidance system for camera calibration based on modelling geometric and corner uncertainty," in *Proceedings of the IEEE/CVF International Conference on Computer Vision*, (2019), pp. 1497–1505.
11. H. Ha, M. Perdoch, H. Alismail, *et al.*, "Deltile grids for geometric camera calibration," in *Proceedings of the IEEE International Conference on Computer Vision*, (2017), pp. 5344–5352.
12. Q. Liu, K. Sun, X. Tang, *et al.*, "Camera calibration based on lightweight fan-shaped target detection and fitness-distance-balance chaotic marine predators algorithm," *Optics Laser Technology* **176**, 110883 (2024).
13. P. Zhou, H. Yin, G. Xu, *et al.*, "Meta-calib: A generic, robust and accurate camera calibration framework with aruco-encoded meta-board," *ISPRS J. Photogramm. Remote. Sens.* **212**, 357–380 (2024).
14. F. Rameau, J. Park, O. Bailo, *et al.*, "Mc-calib: A generic and robust calibration toolbox for multi-camera systems," *Comput. Vis. Image Underst.* **217**, 103353 (2022).
15. J. Heikkila, "Geometric camera calibration using circular control points," *IEEE Trans. Pattern Anal. Machine Intell.* **22**(10), 1066–1077 (2000).
16. F. Yan, Z. Liu, X. Pan, *et al.*, "High-accuracy calibration of cameras without depth of field and target size limitations," *Opt. Express* **28**(19), 27443–27458 (2020).
17. Y. Li, W. Ja, P. Chen, *et al.*, "Extrinsic calibration of non-overlapping multi-camera system with high precision using circular encoded point ruler," *Opt. Lasers Eng.* **174**, 107927 (2024).
18. L. Bu, H. Huo, X. Liu, *et al.*, "Concentric circle grids for camera calibration with considering lens distortion," *Opt. Lasers Eng.* **140**, 106527 (2021).
19. J. Yu, Y. Liu, Z. Zhang, *et al.*, "High-accuracy camera calibration method based on coded concentric ring center extraction," *Opt. Express* **30**(23), 42454–42469 (2022).
20. Z. Meng, H. Zhang, D. Guo, *et al.*, "Defocused calibration for large field-of-view binocular cameras," *Autom. Constr.* **147**, 104737 (2023).
21. J. Rehder, J. Nikolic, T. Schneider, *et al.*, "Extending kalibr: Calibrating the extrinsics of multiple imus and of individual axes," in *2016 IEEE International Conference on Robotics and Automation (ICRA)*, (IEEE, 2016), pp. 4304–4311.
22. D. He, X. Liu, X. Peng, *et al.*, "Eccentricity error identification and compensation for high-accuracy 3d optical measurement," *Meas. Sci. Technol.* **24**(7), 075402 (2013).

23. J. Terven, D.-M. Córdova-Esparza, and J.-A. Romero-González, "A comprehensive review of yolo architectures in computer vision: From yolov1 to yolov8 and yolo-nas," *Mach. Learn. Knowl. Extr.* **5**(4), 1680–1716 (2023).
24. C.-Y. Wang, A. Bochkovskiy, and H.-Y. M. Liao, "Yolov7: Trainable bag-of-freebies sets new state-of-the-art for real-time object detectors," in *Proceedings of the IEEE/CVF conference on computer vision and pattern recognition*, (2023), pp. 7464–7475.
25. J. Redmon, "You only look once: Unified, real-time object detection," in *Proceedings of the IEEE conference on computer vision and pattern recognition*, (2016).
26. S. Agarwal and K. Mierle, "Ceres solver—a large scale non-linear optimization library. 2019,".